Aerospace Science and Technology 143 (2023) 108716

Contents lists available at ScienceDirect

Aerospace Science and Technology

journal homepage: www.elsevier.com/locate/aescte

Assessing the mechanical and static aeroelastic performance of cellular Kirigami wingbox designs

Qinyu Li [a], Oscar Ainsworth [a], Giuliano Allegri [a], Jie Yuan [b], Fabrizio Scarpa [a,*]

[a] Bristol Composites Institute (BCI), Department of Aerospace Engineering, University of Bristol, Bristol BS8 1TR, UK
[b] Department of Aeronautics and Astronautics, University of Southampton, University Road, Southampton SO17 1BJ, UK

ARTICLE INFO

Communicated by Marwan Al-Haik

Keywords:
Kirigami
Micro aerial vehicle (MAV)
Modeling
Metamaterials
Torsional and flexural stiffness
Aeroelasticity

ABSTRACT

Adaptive wings configurations have been evaluated for morphing airframe applications during the last two decades. Constructions with flexible hinges can be in particular a solution for small top medium-scale air vehicles, while novel Kirigami technologies help to produce flexible and complex structures by enabling novel geometric paradigms. In this study, a cellular Kirigami wingbox with an adaptive hinge is designed and manufactured. The mechanical properties of the wingbox are numerically evaluated, considering the shear modulus of the cellular elements patterning the wingbox. Thus, the equivalent torsional, flexural stiffness, as well as the shear center location of the whole wingbox structure are calculated. The analysis is parametrized against various possible internal cell angles and cell thickness values that define the Kirigami cellular tessellation of the wingbox. The static divergence speed is also evaluated by means of the same parametrization. This study shows the feasibility of using a Kirigami wingbox concept for morphing/adaptive small to medium-scale from a structural and aeroelastic perspective.

1. Introduction

Morphing and adaptive airframe configurations have been extensively evaluated during the last three decades, and arguably proposed at a more embryonic stage from the beginning of the aviation era [1]. Adaptive airframe structures have been developed for several platforms, from large scale to Micro Air Vehicles (MAVs) [2]. During the last two decades, MAVs have in particular gained attention for both military and civilian applications, the most promising of these being surveillance and monitoring tasks [3–5]. Designers have attempted to embed features proper to larger aircraft in MAVs, notwithstanding their tight volume constraints. This increases the complexity of design, manufacturing and, partly, operations [6]. The main challenge for fixed-wing small - medium scale air vehicles is the achievement of complex flight envelopes at low Reynolds numbers (within the range of 70,000 to 200,000 for MAVs), and with wings having a small aspect ratio (typically around 1) [7]. The resulting aerodynamic flow can undergo a large separation and reattachment on the top wing surface, creating a separation bubble [8]; this causes a drop in lift and an increase in drag. A low aspect ratio wing at low Reynolds numbers also generates large wingtip vortexes, which interfere with the longitudinal wing circulation [9]. The entrapment of the separated flow causes the occurrence of tip vortex destabilization, which causes instability during roll [9]. Due to their low flight speeds, MAVs are also especially susceptible to wind gusts, which can easily have speeds of the same order of magnitude as the vehicle's flight speed. These problems and a range of flight dynamic issues can be alleviated by introducing a passive wing morphing design within a highly flexible wing structure [10,11]. Novel Kirigami-based manufacturing technologies transform flat sheets into three-dimensional structures. Kirigami manufacturing paradigms provide a unique combination of macro-scale geometry and surface topography [12]. Deployable structures with flexible hinges can be also produced by designing corresponding Kirigami patterns [13–15]. Besides their capacity of being included in passive morphing wings designs, cellular structures possess high flexural stiffness per unit weight and tailorable transverse shear stiffness [11,16–22]. However, the existing literature focuses on the use of cellular/lattice configurations either built as extruded two-dimensional structures or made by elements with tessellations determined by the presence of distributed actuators for the morphing of the wingbox. Aside from the example shown in [23] (and to the best of our knowledge), no other attempt has been made

* Corresponding author.
E-mail addresses: vk18547@bristol.ac.uk (Q. Li), o.ainsworth.2011@my.bristol.ac.uk (O. Ainsworth), giuliano.allegri@bristol.ac.uk (G. Allegri), j.yuan@soton.ac.uk (J. Yuan), f.scarpa@bristol.ac.uk (F. Scarpa).

https://doi.org/10.1016/j.ast.2023.108716
Received 13 June 2023; Received in revised form 15 October 2023; Accepted 31 October 2023
Available online 8 November 2023

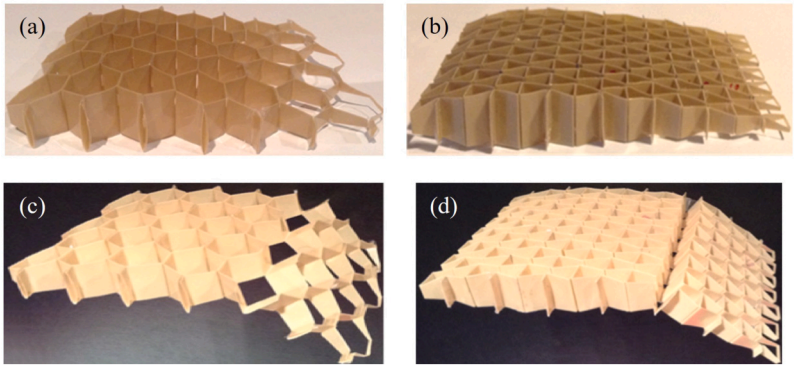

Fig. 1. Examples of Kirigami wingbox cellular structures with (a) hexagonal and (b) re-entrant (butterfly) honeycomb configurations. It is possible to tailor the location of an integrated hinge (c and d) for adaptive shape change performance.

to evaluate the use of Kirigami manufacturing techniques to design and produce integral cellular structures wing boxes, applied in particular to MAV constructions. In this study, we propose a demonstration of the manufacturing and then the parametric analysis of a cellular Kirigami wingbox (section 2). We evaluate the final mass, equivalent shear stiffness, shear center location, and torsional and flexural stiffness for the whole Kirigami cellular wingbox structure as functions of the internal cell angle (section 3.3)and cellular thickness (section 3.4). These analyses are performed by considering the presence (or lack) of an elastomeric skin covering the external surface, which is typical of several morphing wing/airframe configurations [1,4,24]. The static divergence speed is also calculated by varying the cellular geometry configuration (section 3.5). Static divergence is a critical design parameter for flexible wing configurations, as it has been observed since the beginning of heavier-than-air aviation [25].

2. Cellular Kirigami wingbox concept and manufacturing method

2.1. Cellular Kirigami wingbox concept

Morphing wing structures represent viable solutions for MAV designs that achieve good flight dynamics performance [10,11]. Kirigami technologies allow to shape and manufacture the wings with flexible hinges at selected positions to obtain passive morphing and adaptive shape change performance (see Fig. 1). Kirigami is a variation of Origami, the traditional Japanese popular art of paper of folding and cutting paper [12,26]. The Kirigami geometric paradigms allow controlling the cellular configurations and the hinge position. Various centrosymmetric cellular shapes like the hexagonal in Fig. 1(a) and re-entrant in Fig. 1(b) with airfoil cross-sections could be easily available. In order to enable an adaptive shape change, a flexible hinge can be manufactured by partial folding and glueing the flat cut sheet shown in Fig. 1(c) and (d). Cellular structures such as zero Poisson's Ratio honeycomb (ZPR [27]), also allow attaining large in-plane deformations, which are highly beneficial for morphing. Successful applications of morphing structures technologies include wind turbine blades [28], span-wise [24,29,30] and chord-wise morphing [1,31], as well as variable camber wing configurations [32].

2.2. Cellular Kirigami wingbox manufacturing

The basic manufacturing process layout is shown in Fig. 2; the technique described here is similar to the one discussed in a previous work [23]. The first step involves the design of the cutting and folding pattern on the flat sheet in Fig. 2(a) and (d). The material substrate used in this case is PEEK (AZO materials, UK). The second step consists in the curing (thermo forming) of the sheet into a corrugated shape using a mould system made of several aluminum (2024 alloy) rods with trapezium cross-sections. The moulds allow imposing the desired shape of the corrugation on the sheet in Fig. 2(b) and (e). The corrugated part corresponds to the ribbon side in the hexagonal centrosymmetric configurations. The folded and moulded sheet is inserted in a vacuum bag and thermoformed in autoclave for 60 min at 175 °C. The curing corrugated sheets are shown in Fig. 2(c) and (f). The third step involves the folding and glueing of the cured sheets. The glueing at the hinge location should be avoided to make the cellular wingbox flexible in that specific position. Fig. 2 (a), (b) and (c) illustrate the hexagonal (PPR) honeycomb shape; similarly, (d), (e) and (f) correspond to the butterfly (NPR) cellular shape.

3. Numerical evaluation of the wingbox structural properties

3.1. Cellular geometry and Kirigami configuration

A centrosymmetric honeycomb can be considered composed of arrays of unit cells. The geometric and stiffness configuration of the unit cell is responsible for the overall deformation of the honeycomb pane, and, hence its structural response. The unit cell can be entirely described by the lengths h and l, the thickness t, and the internal cell angle θ (Fig. 3). A regular hexagonal unit cell in Fig. 3(a) has a positive internal cell angle; if the internal cell angle is reduced the Poisson's ratio of the honeycomb can be made to decrease. A re-entrant honeycomb in Fig. 3(b) is one where the internal cell angle is negative and as such exhibits a negative Poisson's ratio; if stretched in one direction the honeycomb will now expand in the direction perpendicular to that of the applied displacement. This behavior is known as auxeticity [33–35].

The primary function of a honeycomb sandwich panel is to carry bending loads. Therefore, the honeycomb core, therefore, needs to be suitably stiff to ensure the load transfer between the bending/stretching of the face sheets and the transverse response of the core, which is controlled by the out-of-plane shear modulus. Characterizing the aforementioned parameters is critical for designing a suitable honeycomb core [36]. The out-of-plane shear moduli are given by G_{13} and G_{23}, where the out-of-plane direction is denoted as X_3 and the two in-plane directions are X_1 and X_2, as shown in Fig. 4(a). Two sets of coordinates are employed: the structural "global" reference frame and the "local" coordinate system for the cellular elements. The angle between the two coordinates is marked as φ and the condition shown in Fig. 4(b) is corresponding to $\varphi = 0°$.

The honeycomb shear moduli are complex to calculate, and accurate values can be estimated only via numerical methods. However, upper and lower bounds (Reuss and Voigt bounds) can be computed [36] using complementary and minimum potential energy theorems. For an out-of-plane shear load in the X_1 direction the upper and lower boundaries for the shear modulus G_{13} coincide, giving an exact expression:

$$\frac{G_{13}}{G_s} = \frac{cos\theta}{h/l + sin\theta}\left(\frac{t}{l}\right) \tag{1}$$

where G_s is the shear modulus of the cell wall material given by:

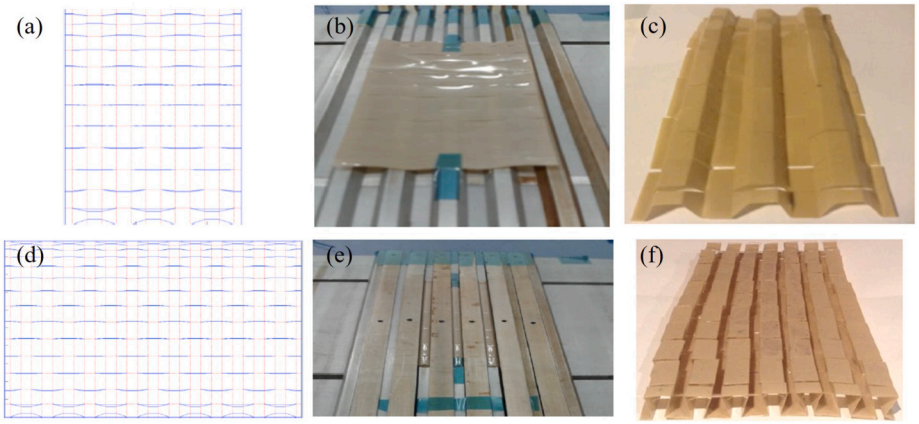

Fig. 2. (a) Pattern of scores and slits for a hexagonal (PPR) honeycomb cellular wingbox; (b) Kirigami PEEK sheet in the mold prior to thermoforming; (c) corrugated template prior to assembly. Figures (d), (e) and (f) are related to a butterfly (NPR) cellular wingbox.

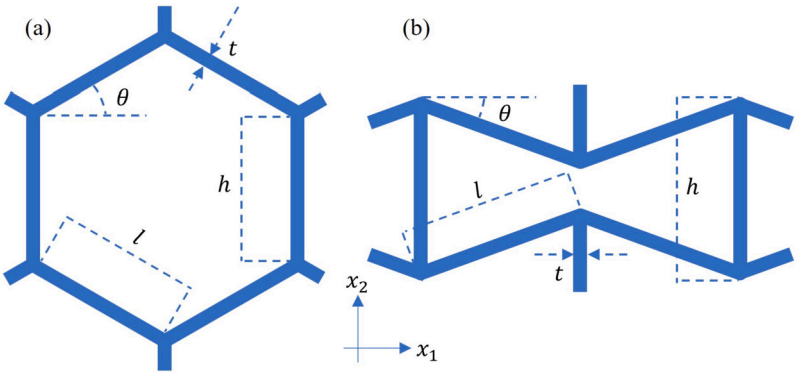

Fig. 3. (a) Hexagonal 2D unit cell with its geometry parameters. (b) An auxetic (butterfly) cell configuration.

$$G_s = \frac{E_s}{2(1+\nu)} \tag{2}$$

where E_s is the elastic modulus of the material. For an out-of-plane shear load in the X_2 direction the upper boundary of G_{23} is determined from: where G_s is the shear modulus of the cell wall material given by:

$$\frac{G_{23}}{G_s} \leq \frac{1}{2}\frac{h/l + 2sin^2\theta}{(h/l + sin\theta)cos\theta}(\frac{t}{l}) \tag{3}$$

The lower boundary of G23 is determined from:

$$\frac{G_{23}}{G_s} \geq \frac{h/l + sin\theta}{(1 + 2h/l)cos\theta}(\frac{t}{l}) \tag{4}$$

In this case, the bounds do not coincide for anything other than a regular hexagonal honeycomb. A finite element simulation is applied to identify an approximated and empirical formula for G_{23} [37]:

$$G_{23} = G_{23_{lower}} + \frac{K}{b/l}(G_{23_{upper}} - G_{23_{lower}}) \tag{5}$$

where

$$K = \begin{cases} 0.788, & \theta \geq 0° \\ 1.342, & \theta < 0° \end{cases} \tag{6}$$

The honeycomb depth is given by b. The parameter K is dependent on the internal cell angle with the auxetic value [38].

3.2. Finite element models

The evaluation of the structural properties is performed using the ANSYS commercial Finite element software (ANSYS, 2013) using APDL language. The geometrical parameters of the unit cell are used to explore the design space for cellular wingbox configurations. The wingbox models are created for a baseline NACA 2415 profile, an aerofoil that has already been successfully used for low-speed MAVs [23,39,40]. The configurations possess both a wingspan and chord length of 0.14 m. For each individual unit cell, the total height and total width are kept constant at 0.021 m, as the internal cell angle is changed the h and l lengths scale accordingly (Fig. 5). This is done to keep the number of cells and overall geometry of the wingbox constant as the unit cell rotations and the internal cell angle are changed. Two types of Kirigami core orientation are considered, one with the unit cell oriented in the manor shown in Fig. 5(a) and (b) labeled as $\varphi = 0°$. In the second configuration, the unit cell rotated 90° as seen in Fig. 5(c) and (d) marked as $\varphi = 90°$.

The wingbox in Fig. 6(a) and (b) features a cellular structure with a transverse torsional stiffness response around the X_2 axis (plane X_1X_3). This arrangement will be from now on referred to as the $\varphi = 0°$ configuration. The wingbox observed in Fig. 6(c) and (d) has its axis of torsion corresponding to the $\varphi = 0°$ configuration. The Kirigami cores are simulated both with and without an elastomeric skin.

The Kirigami wingbox core is simulated using materials properties typical of PEEK; a silicone elastomer of uniform 1 mm thickness is used for the skins (Table 1). Both the honeycomb core and the wingbox skins are modeled using SHELL181 elements, which are four-noded with six Degrees Of Freedom (DOF) at each node (translations in x, y, and z directions, and rotations about the x, y, and z-axes). These elements are suitable for analyzing thin to moderately thick shell structures. A convergence test was performed considering the global torsional and uniaxial deformation of the wingbox according to the boundary conditions described later. The convergence test led to the selection of a maximum element size equal to 1/5 of the l dimension was used. The wingbox core is formed by intersecting a rectangular honeycomb panel with a volume of constant cross-section equal to that of the desired aerofoil extruded along the wingspan. The torsional stiffness GJ is evaluated

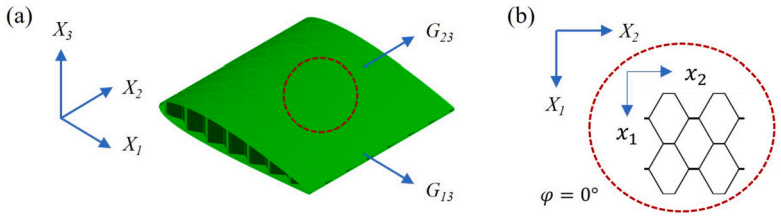

Fig. 4. (a) Global coordinates of the wingbox (b) Local coordinates of the cellular elements.

Table 1
Material properties of the cellular wingbox.

	Material	Young's modulus [MPa]	Poisson's ratio ν	Density ρ [kg/m^3]
Wingbox core	PEEK	$3.95 * 10^3$	0.393	1320
Skin	Silicone	2.83	0.48	1300

by clamping all the degrees of freedom present at the root of the wingbox, while the rotational DOFs around the wingspan axis are coupled together at the tip. At the same tip, a torque M_t is applied at a single node located at the center of the cross-section. A linear elastic static problem is solved resulting in an output rotation θ_t; an approximation of the torsional gradient is calculated as:

$$\frac{d\theta_t}{dz} \simeq \frac{\theta_t}{b} \tag{7}$$

where b is the wingbox span. The torsional stiffness can then be calculated from the classical relation:

$$\frac{GJ}{M_t} = \frac{d\theta_t}{dz} \tag{8}$$

The flexural stiffness EI is evaluated by clamping all DOFs present at the root of the wingbox, while a vertical load P is applied at the shear center of the tip section (to obtain a deflection without twist). Considering the wingbox as a cantilever beam, EI can be calculated using the following formula for an equivalent engineering beam [41]:

$$EI = \frac{PL^3}{3\delta_z} \tag{9}$$

where δ_z is the deflection at the tip in the vertical sense, and L is the wingbox span.

The wingbox mass and center of gravity are provided directly from the postprocessor of the ANSYS FEA code. The shear center though is not, and was instead determined by calculating the point about which the wingbox rotating under pure torsion.

3.3. Internal cell angle variation

The effect of the internal cell angle, θ, has been first investigated within a range of $-40° \leq \theta \leq 40°$. The maximum and minimum values of θ are based on the largest and smallest angles possible before contact of the opposing l length walls becomes an issue. In practice, the maximum internal cell angle would be smaller than the one used, to allow for glueing the h length walls. For the simulations of the configurations with varying θ, the thickness of the core material is kept constant at 0.24 mm.

The two out-of-plane shear moduli corresponding to the parametric cellular cores of the Kirigami models, and responsible for the transverse shear and torsional state were evaluated using the analytical formulas (Eq. (1)-(6)). The results in Fig. 7 (a) have been scaled by the cell wall material shear modulus. It is interesting to note that G_{13} is greater than G_{23} for all values of θ, with the largest value of G_{13} occurring at $\theta = 0°$. It should be noted that if the h and l lengths were the same, isotropic properties would be observed for $\theta = 30°$. The shear center location has been evaluated and shown in Fig. 7(b). The results have been demonstrated in area form and the bottom lines mean the wingbox with 2 mm thickness skin while the top lines stand for the no skin case. The shear center location appears to change with θ; for all models, the most forward position of the shear center occurs at $\theta = 0°$. Both the $\varphi = 0°$ and $\varphi = 90°$ configurations have similar trends, but the $\varphi = 90°$ configuration has a slightly more forward location of the shear center for all values of θ. The addition of skin has little effect on the shear center position, and the latter moves back by at most 5.3% (at $\theta = 40°$ for the $\varphi = 90°$ configuration) with respect to the case where no skin is considered.

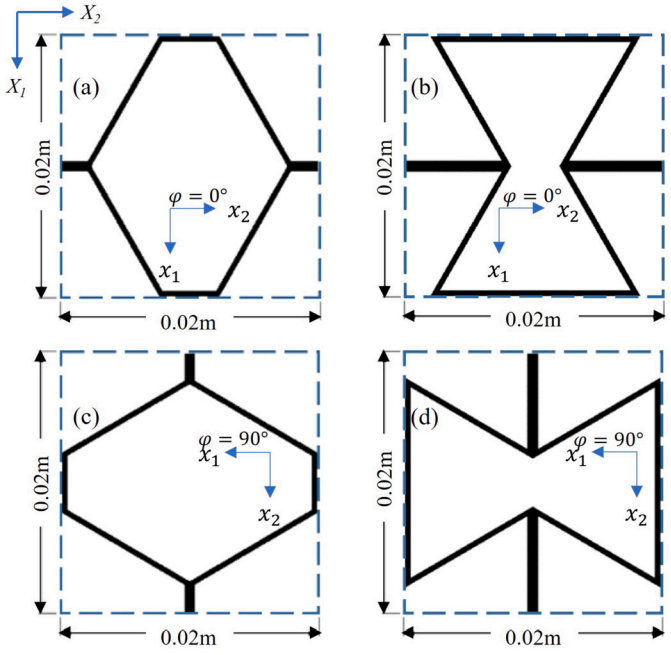

Fig. 5. Unit cell overall size for (a) $\theta = 30°$ $\varphi = 0°$, (b) $\theta = -30°$ $\varphi = 0°$, (c) $\theta = 30°$ $\varphi = 90°$, (d) $\theta = -30°$ $\varphi = 90°$.

The variation of the overall mass of the wingbox versus the internal cell angle is provided in Fig. 7(c). The wingbox mass appears to be directly related to the internal cell angle decreasing, as θ increases. The mass of the wingboxes with the $\varphi = 90°$ unit cell is always slightly larger than the equivalent wingbox with the $\varphi = 0°$ unit cell. As the wingbox size remains constant with the changing θ, the amount of skin and therefore the mass of the skin also stays the same. This shifts upwards the relevant curves, without changing the overall trend. The skin though does contribute significantly to the total mass, from about 4 times at $\theta = -40°$ to 8 times at $\theta = 40°$. The range of the possible shear center locations within the aerofoil is shown in Fig. 7(c) along with the aerodynamic and mass centers (which can be considered approximately constant).

The torsional stiffness GJ is an important mechanical parameter for the aeroelastic design. Fig. 8(a) shows the torsional stiffness for wingboxes with and without the skin. The internal θ angle is again a critical parameter controlling the torsional stiffness of the complete wingbox. This is also confirmed by observing Fig. 8(b), in which a large proportion of the cellular core of the wingbox contributes to the overall

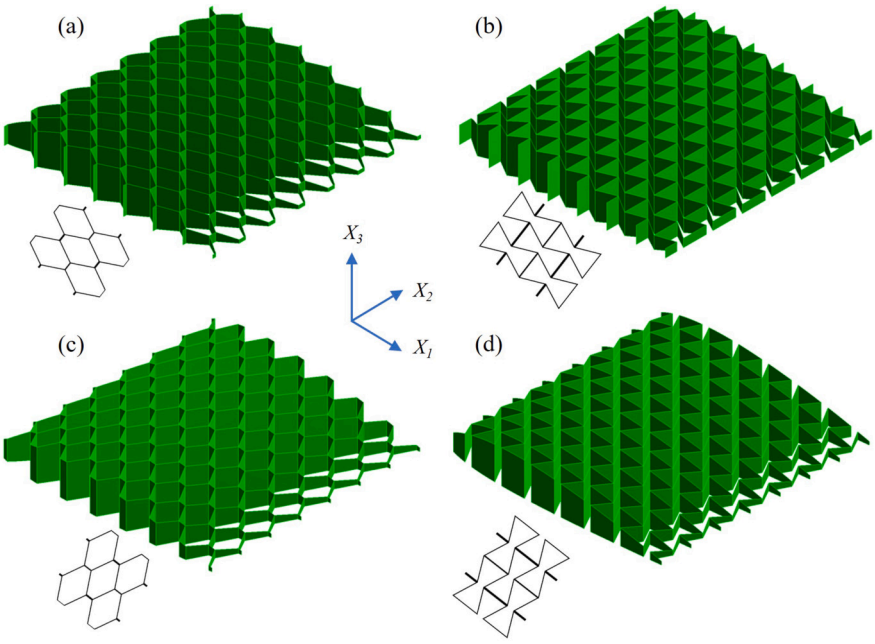

Fig. 6. Wingbox examples with the $\varphi = 0°$ unit cell, (a) for $\theta = 30°$ and (b) for $\theta = -30°$. Similar examples with the same sequence of angles in (c) and (d), this time for configurations with the $\varphi = 90°$ unit cell.

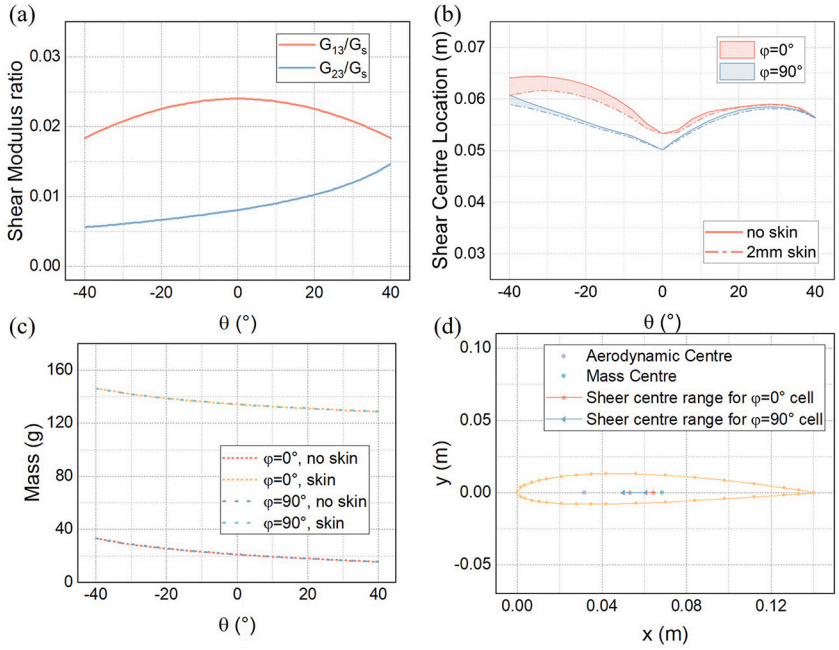

Fig. 7. (a) Shear modulus ratios varying θ. (b) The shear center location along the chord axis relative to the leading edge of the wingbox. The top lines of areas mean no skin cases while the bottom lines stand for 2 mm thick skin cases. (c) The mass trend versus θ. (d) Shear center range and location of the aerodynamic center and mass center for the wingbox with skin.

torsional stiffness, especially for larger positive θ values (95% when $\theta = 40°$) for the $\varphi = 0°$ configuration and more than 99% ($\theta = 0°$) for the $\varphi = 90°$ configuration). On the contrary, negative internal cell angle values give low torsional stiffness and generate cellular cores which contribute less to the overall torsional stiffness (as low as 35% when $\theta = -40°$) for the $\varphi = 0°$ configuration, and as 64% ($\theta = -40°$) for the $\varphi = 90°$ layout). The $\varphi = 90°$ configuration contributes to over 80% of the total torsional stiffness within the range $-36° \leq \theta \leq 40°$; the $\varphi = 0°$ configuration however only provides a similar stiffness contribution for $12° \leq \theta \leq 40°$. Large variations of torsional stiffness with the internal cell angle are possible for the complete wingbox. The torsional stiffness values vary from $31.1 Nm^2$ ($\theta = 40°$) to $0.7 Nm^2$ ($\theta = -40°$) for the $\varphi = 0°$ configuration without skin, and from $79.8 Nm^2$ ($\theta = 0°$) to $4.8 Nm^2$ ($\theta = -40°$) for the $\varphi = 90°$ - again without skin. Of significant interest is the large peak that occurs at $\theta = 0°$ for the $\varphi = 90°$ configuration. The $\theta = 0°$ configuration provides the maximum value of the out-of-plane shear modulus G_{13}/G_c (see Fig. 7 (a)). Also, this internal cell angle configuration makes the honeycomb l length walls align along the length of the wingspan and provide a stretch-dominated response of the cellular core, corresponding to the largest equivalent in-plane moduli. The large in-plane stiffness however occurs for a small internal of internal cell angles ($-5° \leq \theta \leq 5°$) [38]. The effects of the in-plane and shear transverse

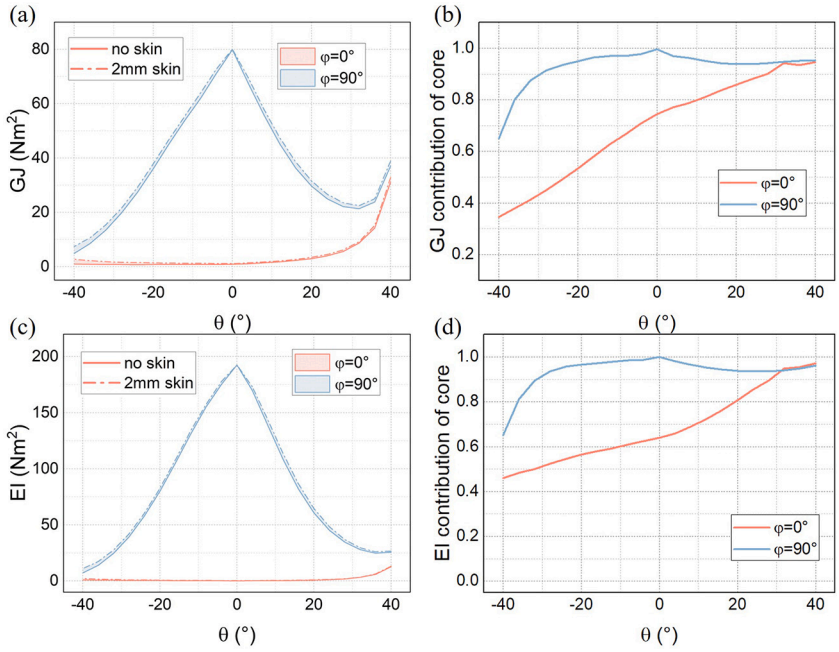

Fig. 8. (a) Trends of the torsional stiffness for wingboxes with and without skin. (b) Core contribution to the total torsional stiffness of the complete wingbox. (c) Flexural stiffness versus θ. (d) Contribution of the core to the total flexural stiffness of the complete wingbox.

stiffness combined together at $\theta = 0°$ to provide the significant peak in torsional stiffness for the $\varphi = 90°$ angle.

The flexural stiffness EI can be also evaluated in Fig. 8(c). Also in this case, the flexural stiffness is directly related to the internal cell angle of the cellular core. The $\varphi = 90°$ configuration wingbox consistently yields the largest EI values, with a significantly higher peak of EI compared to the $\varphi = 0°$ configuration ($192.6 Nm^2$ at $\theta = 0°$, with respect to $11.0 Nm^2$ at $\theta = 40°$ for the wingbox with the skin). The large peak that occurs at $\theta = 0°$ for the $\varphi = 90°$ configuration is again due to the l length walls aligning along the length of the wingspan and therefore providing a large span-wise stiffness. In the case of the $\varphi = 90°$ configuration, the addition of the skin only provides a small increase in terms of flexural stiffness, with the core contribution not dropping below to 80% of the overall wingbox when $-36° \leq \theta \leq 40°$ (see Fig. 8(d)). The flexural stiffness of the $\varphi = 0°$ configuration appears to be greatly affected though by the addition of the skin, with the core contribution only exceeding 80% within $20° \leq \theta \leq 40°$.

3.4. Effect of the variation of the thickness t

Due to the constraints of the Kirigami manufacturing process adopted with its bonding of the moulded ribbons [14], the wall length h is double the thickness of the l walls ($2t$). A thickness range of $0.1mm \leq t \leq 0.8mm$ has been here considered for the parametric simulations related to five different internal cell angles ($\theta = 30°$, $\theta = 15°$, $\theta = 0°$, $\theta = -15°$, $\theta = -30°$). The two out-of-plane shear moduli corresponding to the cellular core composing the Kirigami wingboxes and responsible for the transverse shear and torsional response have been again evaluated using the analytical formulas (Eq. (1)-(6)). The results are shown in Fig. 9(a); the data have been normalized with respect to the shear modulus of the cell wall material. As expected, the shear modulus for all internal cell angles increases linearly with the thickness [36]. In the case of G_{13}/G_s, the $\theta = 0°$ configuration appears the one providing the largest stiffness increase with the thickness. The $-15°$ and $-30°$ internal cell angle configurations have exactly the same response as the 15° and 30° internal cell angles respectively. This is illustrated in Fig. 7(a) [38]. For G_{23}/G_s, the $\theta = 30°$ case is the one showing the largest stiffness increase, while the $\theta = -30°$ case gives the most compliant configuration.

The variation of the wingbox mass for the $\varphi = 0°$ configuration has a positive linear response with increasing wall thickness, no matter the internal cell angle considered (Fig. 9(b)). The configurations with the larger internal cell angles have lower mass, and this holds true as the wall thickness increases. The wingbox size remains constant with the change of the θ angle, and the skin volume remains the same. These two factors contribute to an increase in the slope of the lines, without however changing the overall trend of the mass variation. The case for $\varphi = 90°$ is similar to the one shown in Fig. 7(c); the results related to the $\varphi = 90°$ configurations are therefore not shown here again.

In terms of torsional stiffness GJ, the majority of the cellular wingbox configurations have a stiffness that increases exponentially with the wall thickness for the $\varphi = 0°$ case (Fig. 10(a)). The values of the torsional stiffness for 0°, −15° and −30° are similarly within the same range. Interestingly for the $\varphi = 0°$ cell configuration, an almost linear response is observed (Fig. 10(b)). The Kirigami cellular wingbox at 0° provides the highest torsional stiffness, while the one at −30° features the lowest. The other configurations and the remaining cases follow similar ranges of torsional stiffness. The addition of the skin has a relatively positive effect on the torsional stiffness and this effect decreases as the cell wall thickness increases.

Similarly, the thickness has an almost exponential impact on the flexural stiffness of the Kirigami wingbox configurations with $\varphi = 0°$; the effect becomes however almost linear with the $\varphi = 90°$ cases (Fig. 10(c) and (d)). With the addition of a skin, the $\varphi = 0°$ cell configuration shows a larger relative increase of the flexural stiffness compared to the $\varphi = 90°$ configuration with the skin. The two types of Kirigami cellular wingboxes also share a relative decrease of the effect of the skin over the flexural stiffness as the cell wall thickness increases.

The location of the shear center location is only affected in a negligible manner by the variation of the thickness; the related results are therefore not shown in this section. The internal cell angle appears to be the most critical defining factor. Examples of the total deformation patterns for torsion and bending under unit loads are in Fig. 11 for $\varphi = 90°$ and $\theta = 30°$ for a skin of 2 mm of thickness. Although constrained by the short slenderness of the wing, the deformations associated with the torsion via the pure shear load appear to be distributed in the first 70% of the wingspan starting to the wingtip. Bending however appears to be unfirm only for the first 45% of the wingspan, with both leading

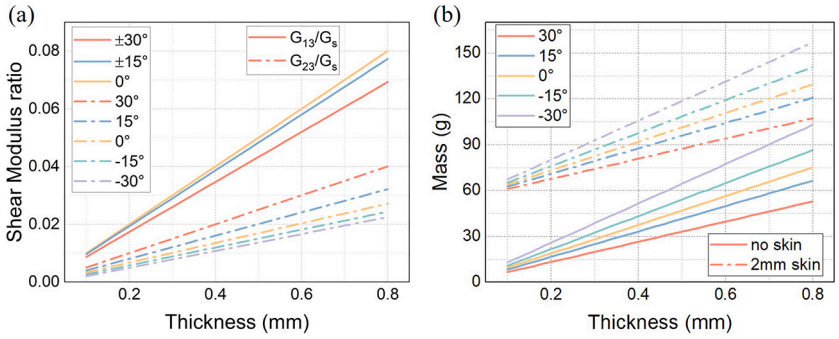

Fig. 9. (a) Evaluation of the shear modulus in the X_1X_3 and X_2X_3 plane. (b) The variation of the wingbox mass for the $\varphi = 0°$ configuration with and without skin.

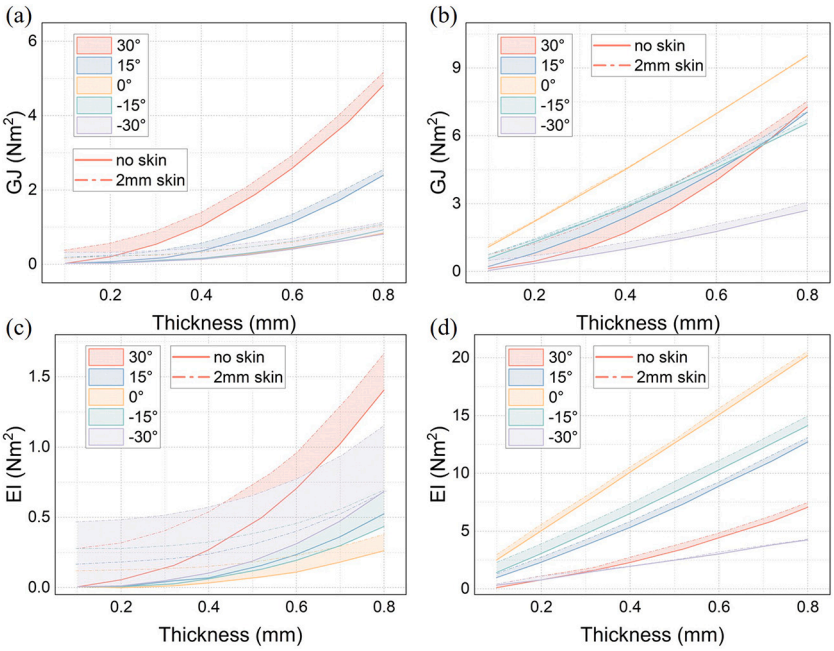

Fig. 10. Variation of the torsional stiffness for the wingboxes; (a) for the $\varphi = 0°$ and (b) for the $\varphi = 90°$ unit cell configurations. Flexural stiffness of the Kirigami wingbox versus the internal cell angle; (c) for the $\varphi = 0°$ and (d) for the $\varphi = 90°$ unit cell configurations.

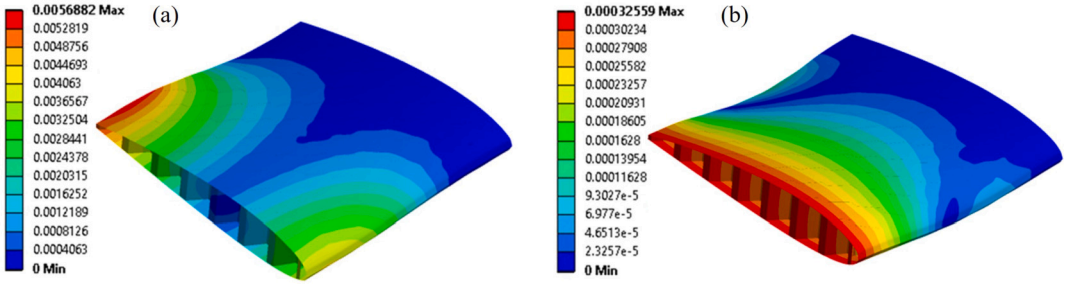

Fig. 11. Total deformation pattern under unit external forces, (a) torsion and (b) bending. Kirigami wiggbox configuration with $\varphi = 90°$ and $\theta = 30°$.

edge and trailing edge showing fields of deformations affected by the clamping of the wing root.

3.5. Aeroelasticity

The static torsional divergence speed is calculated as a first step to assess the aeroelastic properties of the wingboxes. The divergence speed V_d is given by [41]:

$$V_d = \sqrt{\frac{2K}{\rho Sec(\partial C_L/\partial C_\alpha)}} \tag{10}$$

where K is the GJ/d_z torsional stiffness of the wing (dz being the wingspan), S and ρ represent the surface of the wing and the density of air respectively, and ec is the distance between the aerodynamic and the shear centers expressed in terms of the wing chord. The term $\partial C_L/\partial C_\alpha$ is the wing lift curve slope. It can be seen from Eq. (10), it is desirable to maximize GJ and to minimize ec to increase the divergence speed.

The divergence speed was calculated assuming a two-dimensional lift curve slope ($\partial C_L/\partial\alpha$) of 2π, an air density of 1.225 kg/m^3, and an aerodynamic center of 0.245 [9]. The unit cell angles of the Kirigami wingbox configurations are critical factors in determining the divergence speed. Fig. 12(a) shows in particular that the variation of the

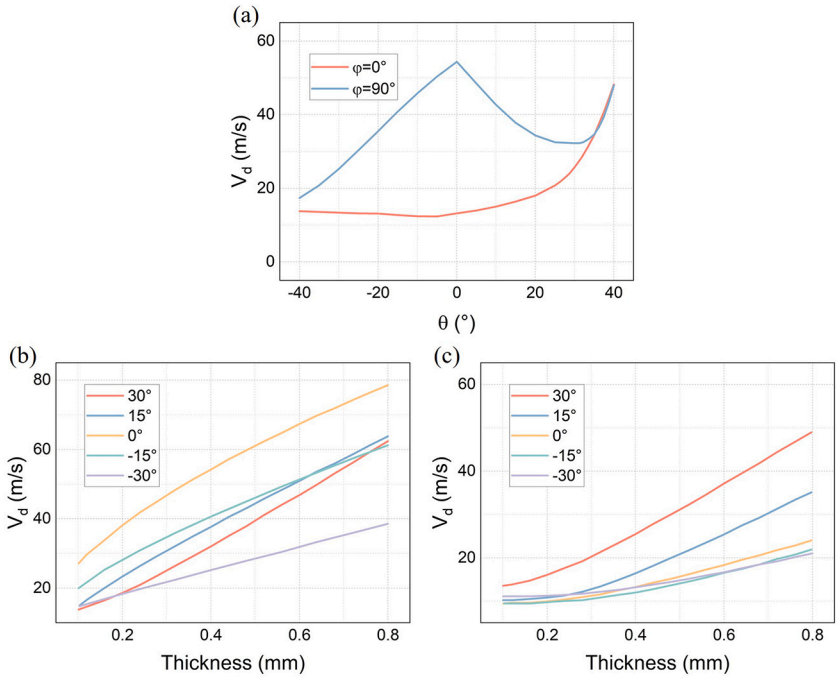

Fig. 12. (a) Variation of the divergence speed with the internal cell angle ($t = 0.4mm$). (b) Divergence speed with respect to the cell wall material thickness and for (b) $\varphi = 0°$ and (c) for $\varphi = 90°$ unit cell configurations.

internal cell allows for ranges of values of the divergence speed as large as $12m/s \leq V_d \leq 48m/s$ for the $\varphi = 0°$ unit cell configuration; the range of velocities spans within $17m/s \leq V_d \leq 54m/s$ for the $\varphi = 0°$ cell layout. The largest value of divergence speed is observed for the $\varphi = 0°$ wingbox configuration at $\theta = 0°$; this is because that geometry of the wingbox features both the largest torsional stiffness (Fig. 8(a)) and the most forward position of the shear center (Fig. 7(b)). As expected, the presence of the skin provides an increase in the divergence speed (Figs. 12 (b) and (c)), although the trend is not purely linear because of the way the variation of the total mass of the wingbox varies with the skin thickness (see Fig. 9 (b)). The cellular wingbox configurations shown here are based on the shaping of centrosymmetric honeycomb configurations around a specific airfoil using Kirigami techniques. The use of positive and negative internal cell angles affects the distribution and magnitude of the shear stresses in the honeycomb walls across the thickness. Smith and Scarpa [42] showed that honeycombs with $\vartheta = +-10°$ show variations of 50% of the intensity of the maximum stresses for thickness ratios up to $t/l = 8$, with the largest values for the auxetic configuration. Thinner honeycombs ($t/l = 2$) have however less than 10% of variation. In that sense, Kirigami cellular wingboxes made for thin airfoils would be less susceptible to the internal cell angle when shear stress concentrations during bending and torsional loading are considered. A way to significantly reduce stress concentrations no matter the honeycomb thickness is to adopt lattice configurations with curved walls/ligaments [43]. In that sense, centrosymmetric honeycombs with walls served by ligaments with radius offer a significant reduction of the peak shear stresses and strains and lower overall values of Voigt/Reuss bounds [44][44]. An aspect to consider, however, is that the use of honeycombs with curved cells further increases torsional compliance. Also, the peak of the transverse shear modulus is at $\vartheta = 0°$ with the honeycombs with sharp wall junctions used in this work. The presence of radius in the curved wall honeycombs would shift that peak and change the overall bending and torsional stiffness of the Kirigami wingbox [45]. Another way to increase the stiffness and strength of the cellular structure is to use polymeric inserts at the intersection of the honeycomb cell walls [46], a strategy that has also been adopted to assemble Kirigami zero Poisson's ratio honeycombs made from PEEK films [47]. While this solution may provide an increase to the overall weight of the cellular wingbox, it may provide however a good trade-off between specific shear moduli and shear strength for the cellular structure making the Kirigami wingbox [47].

4. Conclusion

This work has described the manufacturing and parametric design of cellular wingbox structured made via Kirigami techniques. A parametric analysis has explored the design space of these wingboxes in terms of static mechanical and aeroelastic divergence. The Kirigami cellular configurations can be tailored by changing the unit cell angles, while keeping the thickness and overall sizing constrained by the manufacturing process adopted. A parametric Finite Element Analysis shows that the torsional stiffness, flexural stiffness and shear center location could be significantly varied by tuning the internal cell angles. Moreover, the equivalent torsional and flexural stiffnesses of the wingboxes could also be varied through the cell wall thickness. Both torsional stiffness and locations of the shear center could be varied to provide large ranges of divergence speeds. Of particular interest is found to be the $\varphi = 90°$ unit cell wingbox configuration, which provides the largest torsional and flexural stiffness values, as well as the most forward shear center location for the same internal cell angle of $\theta = 0°$. Kirigami wingbox constructions are feasible and scalable and provide a way to tailor static and aeroelastic structural properties of MAV and potentially medium scale wing assemblies.

Declaration of competing interest

The authors declare that they have no known competing financial interests or personal relationships that could have appeared to influence the work reported in this paper.

Data availability

Data will be made available on request.

Acknowledgements

QL is grateful for the support provided by the Faculty of Engineering of the University of Bristol. FS acknowledges the support of the FP7-NMP-246067 M-RECT project. FS, QL and GA acknowledge the partial support from the JTI-CS2-2018-CfP09-LPA-01-60 865007 InnoSTAT programme.

References

[1] Silvestro Barbarino, Farhan Gandhi, Steven D. Webster, Design of extendable chord sections for morphing helicopter rotor blades, J. Intell. Mater. Syst. Struct. 22 (9) (2011) 891–905.
[2] James M. McMichael, Micro air vehicles-toward a new dimension in flight, http://www.arpa.gov/tto/MAV/mav_auvsi.html, 1997.
[3] Mario Coppola, Kimberly N. McGuire, Christophe De Wagter, Guido C.H.E. De Croon, A survey on swarming with micro air vehicles: fundamental challenges and constraints, Front. Robot. AI 7 (18) (2020).
[4] Spoorthi Singh, Mohammad Zuber, Mohd Nizar Hamidon, Norkhairunnisa Mazlan, Adi Azriff Basri, Kamarul Arifin Ahmad, Classification of actuation mechanism designs with structural block diagrams for flapping-wing drones: a comprehensive review, Prog. Aerosp. Sci. 132 (2022) 100833.
[5] Taimur Ali Shams, Syed Irtiza Ali Shah, Ali Javed, Syed Hossein Raza Hamdani, Airfoil selection procedure, wind tunnel experimentation and implementation of 6DOF modeling on a flying wing micro aerial vehicle, Micromachines 11 (6) (2020) 553.
[6] Luca Petricca, Per Ohlckers, Christopher Grinde, Micro- and nano-air vehicles: state of the art, Int. J. Aerosp. Eng. (2011) 2011.
[7] Bret Kennedy Stanford, Aeroelastic Analysis and Optimization of Membrane Micro Air Vehicle Wings, University of Florida, 2008.
[8] H.P. Horton, A.D. Young, Some Results of Investigations of Separation Bubbles (Flow Separation Bubble Data, and Comparisons with Velocity and Pressure Measurements), vol. 1966, 1966, pp. 779–811.
[9] Thomas J. Mueller, Gabriel E. Torres, Aerodynamics of low aspect ratio wings at low Reynolds numbers with applications to micro air vehicle design and optimization, Technical report, Notre Dame Univ in Office of Research, 2001.
[10] Jian Sun, Qinghua Guan, Yanju Liu, Jinsong Leng, Morphing aircraft based on smart materials and structures: a state-of-the-art review, J. Intell. Mater. Syst. Struct. 27 (17) (2016) 2289–2312.
[11] Jian Sun, Linzhe Du, Fabrizio Scarpa, Yanju Liu, Jinsong Leng, Morphing wingtip structure based on active inflatable honeycomb and shape memory polymer composite skin: a conceptual work, Aerosp. Sci. Technol. 111 (2021) 106541.
[12] Sebastien JP Callens, Amir A. Zadpoor, From flat sheets to curved geometries: origami and Kirigami approaches, Mater. Today 21 (3) (2018) 241–264.
[13] Taketoshi Nojima, Kazuya Saito, Development of newly designed ultra-light core structures, JSME Int. J. Ser. A, Solid Mech. Mater. Eng. 49 (1) (2006) 38–42.
[14] Taketoshi Nojima, et al., Origami Modeling of Functional Structures Based on Organic Patterns, Kyoto University, 2002.
[15] Robin M. Neville, Fabrizio Scarpa, Alberto Pirrera, Shape morphing Kirigami mechanical metamaterials, Sci. Rep. 6 (1) (2016) 31067.
[16] R.M. Ajaj, E.I. Saavedra Flores, M.I. Friswell, G. Allegri, B.K.S. Woods, A.T. Isikveren, W.G. Dettmer, The zigzag wingbox for a span morphing wing, Aerosp. Sci. Technol. 28 (1) (2013) 364–375.
[17] D. Bornengo, F. Scarpa, C.D.L.R. Remillat, Evaluation of hexagonal chiral structure for morphing airfoil concept, Proc. Inst. Mech. Eng., G J. Aerosp. Eng. 219 (3) (2005) 185–192.
[18] Hyeonu Heo, Jaehyung Ju, Doo-Man Kim, Compliant cellular structures: application to a passive morphing airfoil, Compos. Struct. 106 (2013) 560–569.
[19] Jamie Martin, Jean-Jacques Heyder-Bruckner, Chrystel Remillat, Fabrizio Scarpa, Kevin Potter, Massimo Ruzzene, The hexachiral prismatic wingbox concept, Phys. Status Solidi B 245 (3) (2008) 570–577.
[20] Enrico Cestino, Tuba Majid, Bruce W. Jo, Status and challenges on design and implementation of camber morphing mechanisms, Int. J. Aerosp. Eng. 2021 (2021) 6399937.
[21] B. Jenett, S. Calisch, D. Cellucci, N. Cramer, N. Gershenfeld, S. Swei, K.C. Cheung, Digital morphing wing: active wing shaping concept using composite lattice-based cellular structures, Soft Robot. 4 (2017) 33–48.
[22] N.M. Wereley, P.C. Chen, E.A. Bubert, C.S. Kothera, B.K.S. Woods, Cellular support structures used for controlled actuation of fluid contact surfaces, 2007, US Patent US7931240B2.
[23] Kazuya Saito, Fabio Agnese, Fabrizio Scarpa, A cellular Kirigami morphing wingbox concept, J. Intell. Mater. Syst. Struct. 22 (9) (2011) 935–944.
[24] Edward A. Bubert, Benjamin K.S. Woods, Keejoo Lee, Curt S. Kothera, N.M. Wereley, Design and fabrication of a passive 1D morphing aircraft skin, J. Intell. Mater. Syst. Struct. 21 (17) (2010) 1699–1717.
[25] R.L. Bisplinghoff, H. Ashley, R.L. Halfman, Aeroelasticity, Dover Science, 1996.
[26] Zirui Zhai, Lingling Wu, Hanqing Jiang, Mechanical metamaterials based on origami and Kirigami, Appl. Phys. Rev. 8 (4) (2021) 041319.
[27] Weidong Liu, Honglin Li, Zhendong Yang, Jiong Zhang, Cenbo Xiong, Mechanics of a novel cellular structure for morphing applications, Aerosp. Sci. Technol. 95 (2019) 105479.
[28] Xavier Lachenal, Stephen Daynes, Paul M. Weaver, Review of morphing concepts and materials for wind turbine blade applications, Wind Energy 16 (2) (2013) 283–307.
[29] Robert D. Vocke III, Curt S. Kothera, Benjamin K.S. Woods, Norman M. Wereley, Development and testing of a span-extending morphing wing, J. Intell. Mater. Syst. Struct. 22 (9) (2011) 879–890.
[30] Robert Vocke, Curt Kothera, Norman Wereley, Development of a span-extending blade tip system for a reconfigurable helicopter rotor, in: 53rd AIAA/ASME/ASCE/AHS/ASC Structures, Structural Dynamics and Materials Conference 20th AIAA/ASME/AHS Adaptive Structures Conference 14th AIAA, 2012, p. 1664.
[31] Weidong Liu, Hua Zhu, Shengqiang Zhou, Yalei Bai, Yuan Wang, Chunsheng Zhao, In-plane corrugated cosine honeycomb for 1D morphing skin and its application on variable camber wing, Chin. J. Aeronaut. 26 (4) (2013) 935–942.
[32] Stephen Daynes, P.M. Weaver, Design and testing of a deformable wind turbine blade control surface, Smart Mater. Struct. 21 (10) (2012) 105019.
[33] Wei Yang, Zhong-Ming Li, Wei Shi, Bang-Hu Xie, Ming-Bo Yang, Review on auxetic materials, J. Mater. Sci. 39 (2004) 3269–3279.
[34] Chen Luo, Chuan Zhen Han, Xiang Yu Zhang, Xue Gang Zhang, Xin Ren, Yi Min Xie, Design, manufacturing and applications of auxetic tubular structures: a review, Thin-Walled Struct. 163 (2021) 107682.
[35] Wei Jiang, Xin Ren, Shi Long Wang, Xue Gang Zhang, Xiang Yu Zhang, Chen Luo, Yi Min Xie, Fabrizio Scarpa, Andrew Alderson, Ken E. Evans, Manufacturing, characteristics and applications of auxetic foams: a state-of-the-art review, Composites, Part B, Eng. (2022) 109733.
[36] S. Kelsey, R.A. Gellatly, B.W. Clark, The shear modulus of foil honeycomb cores: a theoretical and experimental investigation on cores used in sandwich construction, Aircr. Eng. Aerosp. Technol. (1958).
[37] M. Grediac, A finite element study of the transverse shear in honeycomb cores, Int. J. Solids Struct. 30 (13) (1993) 1777–1788.
[38] F. Scarpa, G. Tomlinson, On static and dynamic design criteria of sandwich plate structures with a negative Poisson's ratio core, Appl. Mech. Eng. 5 (1) (2000) 207–222.
[39] Soylak Mustafa, Experimental investigation of aerodynamic performance of oscillating wings at low Re numbers, Proc. Inst. Mech. Eng., G J. Aerosp. Eng. 230 (10) (2016) 1882–1902.
[40] M. Serdar Genç, Ünver Kaynak, Hüseyin Yapici, Performance of transition model for predicting low Re aerofoil flows without/with single and simultaneous blowing and suction, Eur. J. Mech. B, Fluids 30 (2) (2011) 218–235.
[41] Thomas Henry, Gordon Megson, Aircraft Structures for Engineering Students, Elsevier, 2007.
[42] Francis Smith, Fabrizio Scarpa, Design of honeycomb-like composites for electromagnetic and structural applications, IEE Proc. Sci. Meas. Technol. 151 (2004) 9–15.
[43] Kusum Meena, Sarat Singamneni, A new auxetic structure with significantly reduced stress concentration effects, Mater. Des. 173 (2019) 107779.
[44] A. Harkati, D. Boutagouga, E. Harkati, A. Bezazi, F. Scarpa, M. Ouisse, In-plane elastic constants of a new curved cell walls honeycomb concept, Thin-Walled Struct. 149 (2020) 106613.
[45] Amine Harkati, El Haddi Harkati, Abderrezak Bezazi, Fabrizio Scarpa, Morvan Ouisse, Out-of-plane elastic constants of curved cell walls honeycombs, Compos. Struct. 268 (2021) 113959.
[46] M.-A. Boucher, C.W. Smith, F. Scarpa, R. Rajasekaran, K.E. Evans, Effective topologies for vibration damping inserts in honeycomb structures, Compos. Struct. 106 (2013) 1–14.
[47] R.M. Neville, A. Monti, K. Hazra, F. Scarpa, C. Remillat, I.R. Farrow, Transverse stiffness and strength of Kirigami zero-ν peek honeycombs, Compos. Struct. 114 (2014) 30–40.